PNAS RESEARCH ARTICLE | PHYSICS

Bulk and surface Dirac states accompanied by two superconducting domes in FeSe-based superconductors

Qiang Hou[a,1], Wei Wei[a,1], Xin Zhou[a], Wenhui Liu[a], Ke Wang[a], Xiangzhuo Xing[b], Yufeng Zhang[c], Nan Zhou[d], Yongqiang Pan[d], Yue Sun[a,2], and Zhixiang Shi[a,2]

Affiliations are included on p. 6.

Edited by Subir Sachdev, Harvard University, Cambridge, MA; received May 15, 2024; accepted October 22, 2024

Recent investigations of FeSe-based superconductors have revealed the presence of two superconducting domes and suggest possible distinct pairing mechanisms. Two superconducting domes are commonly found in unconventional superconductors and exhibit unique normal states and electronic structures. In this study, we conducted electromagnetic transport measurements to establish a complete phase diagram, successfully observing the two superconducting domes in $FeSe_{1-x}S_x$ ($0 \le x \le 0.25$) and $FeSe_{1-x}Te_x$ ($0 \le x \le 1$) superconductors. The normal state resistivity on SC1 shows the strange metal state, with a power exponent approximately equal to 1 ($\rho(T) \propto T^n$ with $n \sim 1$), whereas the exponent on SC2 is less than 1. A bulk Dirac state observed on SC1, completely synchronized with the strange metal behavior, indicating a close relationship between them. While a topological surface Dirac state is witnessed on SC2 and undergoes a sign change near the pure nematic quantum critical point. The evolution of the Dirac states indicates that the appearance of the two superconducting domes may originate from the Fermi surface reconstruction. Our findings highlight distinct Dirac states and normal state resistivity across the two superconducting domes, providing convincing evidence for the existence of the two different pairing mechanisms in FeSe-based superconductors.

FeSe-based superconductors | two superconducting domes | Dirac states | strange metal

Significance

Two superconducting domes are commonly found in unconventional superconductors, such as cuprates, iron-based compounds, and heavy fermions. The superconducting dome close to the order state of the parent phase is often accompanied by magnetic quantum critical point (QCP), while the other superconducting dome far away from the ordered state is closely related to non-Fermi liquid. Interestingly, the two superconducting domes found in FeSe-based superconductors exhibit unique normal state resistivity and pure nematic QCP. The evolution of the Dirac states indicates that the two superconducting domes have different electronic structures. These results support the possibility of two different pairing mechanisms in FeSe-based superconductors, providing valuable clues for studying these two superconducting domes.

Two superconducting domes are commonly found in unconventional superconductors, such as cuprates (1–3), iron-based compounds (4, 5), and heavy fermions (6). These two superconducting domes are unconventional and often share some common properties. The dome close to the ordered state has lower superconducting transition temperature (T_c), and the higher T_c dome with non-Fermi liquid is far away from the ordered state (7–9). Non-Fermi liquid and quantum critical point (QCP) are generally decoupled and well separated (10, 11). These properties are summarized into a universal phase diagram and become the paradigm of the two superconducting domes in unconventional superconductors (12).

Recently, it has been reported that the two superconducting domes are found in FeSe-based superconductors, which may have different pairing mechanisms (13, 14). Specifically, the superconducting dome SC1 near FeSe is mediated by the antiferromagnetic (AFM) fluctuations, whereas SC2 near $FeSe_{0.5}Te_{0.5}$ is associated with the pure nematic fluctuations. Although FeSe exhibits a nematic phase without long-range magnetic order below ~90 K, several magnetic measurements have detected stripe-type AFM fluctuations within the nematic phase (15, 16). With S doping and the application of pressure, the influence of the nematic fluctuations on T_c is limited, while spin fluctuations play a more significant role (17–19). For SC2, elastoresistivity studies have demonstrated that $FeSe_{1-x}Te_x$ crosses a nonmagnetic pure nematic QCP, and the enhancement of superconductivity can be attributed to the nematic fluctuations (13, 20). The shrinkage of the superconducting domes under high magnetic fields further supports that SC1 and SC2 are mediated by AFM fluctuations and nematic fluctuations, respectively (14). The paradigm and electronic structure of the two superconducting domes are crucial to the exploration of the unconventional superconducting pairing mechanism.

FeSe is a compensated semimetal with the equal numbers of electron and hole carriers, in which hole pockets exist in the center of the Brillouin zone and electron pockets exist in the corners of the Brillouin zone (26). Especially in the nematic phase, the electron-type bulk Dirac cone is found at the Brillouin zone corner (27). On the other hand, the normal state within the nematic phase of FeSe exhibits a good strange metal behavior, i.e., non-Fermi liquid (21, 28). The study of $FeSe_{1-x}S_x$ under high fields suggests that the origin of the Dirac state may be related to strange metals (22). Te substitution enhances the spin–orbit coupling (SOC), resulting in topologically nontrivial surface Dirac cones

Author contributions: Q.H., Y.S., and Z.S. designed research; Q.H., W.W., X.Z., W.L., K.W., X.X., Y.Z., N.Z., and Y.P. performed research; Q.H., W.W., Y.S., and Z.S. analyzed data; and Q.H., W.W., and Y.S. wrote the paper.

The authors declare no competing interest.

This article is a PNAS Direct Submission.

[1]Q.H. and W.W. contributed equally to this work.

[2]To whom correspondence may be addressed. Email: sunyue@seu.edu.cn or zxshi@seu.edu.cn.

This article contains supporting information online at https://www.pnas.org/lookup/suppl/doi:10.1073/pnas.2409756121/-/DCSupplemental.

Published November 21, 2024.

characterized by a band inversion along the Γ–Z line of the Brillouin zone, which has also been confirmed in magnetotransport measurements (29–31). When the system becomes superconducting, these topological surface Dirac states could become gapped due to the proximity effect with the bulk superconductivity, leading to the formation of topological superconductivity (29). Understanding the electronic structure is pivotal for unraveling the pairing mechanism. Due to challenges in sample preparation and measurement, previous research on the Dirac states has been confined to FeSe and the Te higher region. Consequently, the evolution from the bulk Dirac states to the topological surface Dirac states is still unclear. The study of the Dirac states and the normal state resistivity is crucial for the unconventional superconducting pairing mechanisms, particularly for SC2 associated with the pure nematic QCP.

Electromagnetic transport stands as a convenient and efficient method for detecting superconductivity and electronic structure. In this study, high-quality $FeSe_{1-x}Te_x$ ($0 \le x \le 1$) single crystals were successfully synthesized, with sizes reaching several mm^2. We have established a temperature-doping phase diagram and observed the two superconducting domes, SC1 and SC2, as shown in Fig. 1 (See *SI Appendix*, Figs. S1 and S2 for additional details on $FeSe_{1-x}Te_x$, the data on $FeSe_{1-x}S_x$ are from relevant references). The normal state on SC1 far from the long-range AFM order at FeTe exhibits a non-Fermi liquid state, and the T_c is smaller than that of SC2 close to the AFM order. According to the comprehensive analysis of Hall resistivity and magnetoresistance (MR), we propose that there are three kinds of the Dirac states, the electron-type bulk Dirac state at the Brillouin zone corner, the hole- and electron-type surface Dirac states characterized by a band inversion along the Γ–Z line. The topologically trivial bulk and topologically nontrivial surface Dirac states are accompanied by SC1 and SC2, respectively, suggesting that the origin of the two superconducting domes is due to the change in electronic structure, which is consistent with many previous researches (32, 33). Our findings indicate that the two superconducting domes in FeSe-based superconductors are naturally the same as those in other unconventional superconductors (12), and the stark contrast between the Dirac states and the normal state resistivity of the two superconducting domes supports the possibility of two different pairing mechanisms.

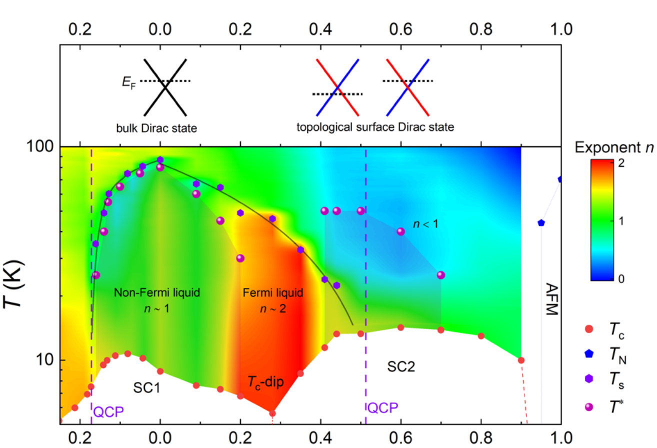

Fig. 1. Evolution phase diagram of the Dirac states, superconductivity, magnetic order, and crystal structure with S and Te doping for $FeSe_{1-x}S_x$ and $FeSe_{1-x}Te_x$single crystals. T^* is the critical temperatures below which the Dirac states appear, T_N is the Néel temperature, T_c is the superconducting transition temperature, and T_s is the structural (nematic) transition temperature. The temperature dependence of the exponent n extracted from $d\ln(\rho - \rho_0)/d\ln T$ for each crystal is represented as a contour plot. T^*, T_s, T_c, and n in $FeSe_{1-x}S_x$ ($0 < x \le 0.25$) are from refs. 16, and 21–25. The purple dashed line represents the nematic QCP near x(S) ~ 0.17 (25) and x(Te) ~ 0.52 (13, 14). Three schematic diagrams of Dirac states in top panel, namely the electron bulk Dirac state, the hole and electron topological surface Dirac states, in which the black dashed line is the Fermi surface, and the intersection of the red and blue solid lines represents the topological surface Dirac state characterized by the band inversion.

Results

Fig. 2 presents the magnetic field dependence of the Hall resistivity $\rho_{xy}(H)$ at various temperatures for $FeSe_{1-x}S_x$ ($0 < x \le 0.21$) and $FeSe_{1-x}Te_x$ ($0 \le x \le 1$) single crystals. FeSe exhibits clear nonlinear behavior with a concave shape at low temperatures below 80 K, which has been ascribed to the emergence of the minority electron carriers with high mobility (34–36). The angle-resolved photoemission spectroscopy (ARPES) results of FeSe show that these minority electron bands with high mobility are the topologically trivial electronic bulk Dirac cones appearing around the Brillouin zone corner (27, 37–39). This nonlinear behavior gradually diminishes with S or Te doping and becomes linear at x(S) = 0.21 or x(Te) = 0.28, indicating that the bulk Dirac states are gradually suppressed until they disappear.

An interesting phenomenon occurs when the Te content increases to the range of 0.41 to 0.5: the nonlinear Hall behavior reappears, but with a convex shape. For x(Te) = 0.6, the nonlinear Hall behavior becomes concave again, which is attributed to the electron Dirac state (40). The ARPES results of $FeSe_{0.45}Te_{0.55}$ shows that, unlike FeSe, topologically nontrivial surface Dirac states of the Brillouin zone are induced due to the enhancement of SOC by Te substitution (29). Compared to the concave shape in x(Te) = 0.6, the nonlinear convex behavior can be naturally ascribed to the hole topological surface Dirac state based on the compensation effect in the whole $FeSe_{1-x}Te_x$ system. The compensated semimetal characteristic has been verified through various experiments, such as thermoelectric properties (41, 42), ARPES (31, 43–46), and Hall coefficients R_H at small fields (*SI Appendix*, Fig. S3). In order to provide the distribution of the Dirac states in FeSe-based superconductors, we define the characteristic temperature T^* as the temperature at which nonlinear $\rho_{xy}(H)$ is observed just before the transition to linear behavior, representing the emergence of Dirac states (see *SI Appendix*, Fig. S4 for the selection method). These T^* values are summarized in Fig. 1. It should be emphasized that the variation in T^* due to this selection has minimal impact on the phase diagram and the conclusions of our work. Moreover, at x(Te) = 0.8 and 0.9, the Hall effects become linear, and the Hall coefficients remain positive without sign changes. In the case of FeTe, the Hall resistivity is linear, but the Hall coefficient changes from positive to negative below 70 K, which can be attributed to the AFM transition (47).

It is well known that MR linearly dependent on magnetic field is one of the macroscopic manifestations of the Dirac state (50, 51). In order to further verify the evolution of the Dirac states with S or Te doping based on the Hall effects, we conducted MR measurements. Fig. 3 displays the magnetic field dependence of MR, $\Delta\rho/\rho_0 = (\rho_{xx}(H) - \rho_{xx}(0))/\rho_{xx}(0)$, and the first-order derivative of the MR to the magnetic field, d(MR)/dH, at different temperatures for $FeSe_{1-x}S_x$ ($0 < x \le 0.21$) and $FeSe_{1-x}Te_x$ ($0 \le x \le 0.6$) single crystals. In the case of crystals with $0.7 \le x(\mathrm{Te}) \le 1$, the MR values are on the order of one thousandth and nearly zero, making the quantitative analysis unreliable. Therefore, we only analyze the MR data at $0 < x(\mathrm{S}) \le 0.21$ and $0 \le x(\mathrm{Te}) \le 0.6$. For FeSe, the MR value is approximately 60% at 15 K and 9T, and it gradually decreases as the temperature increases. However, the MR value is suppressed to less than 20% for the S-doped crystals and less than 5% for the Te-doped crystals due to the enhancement of scattering.

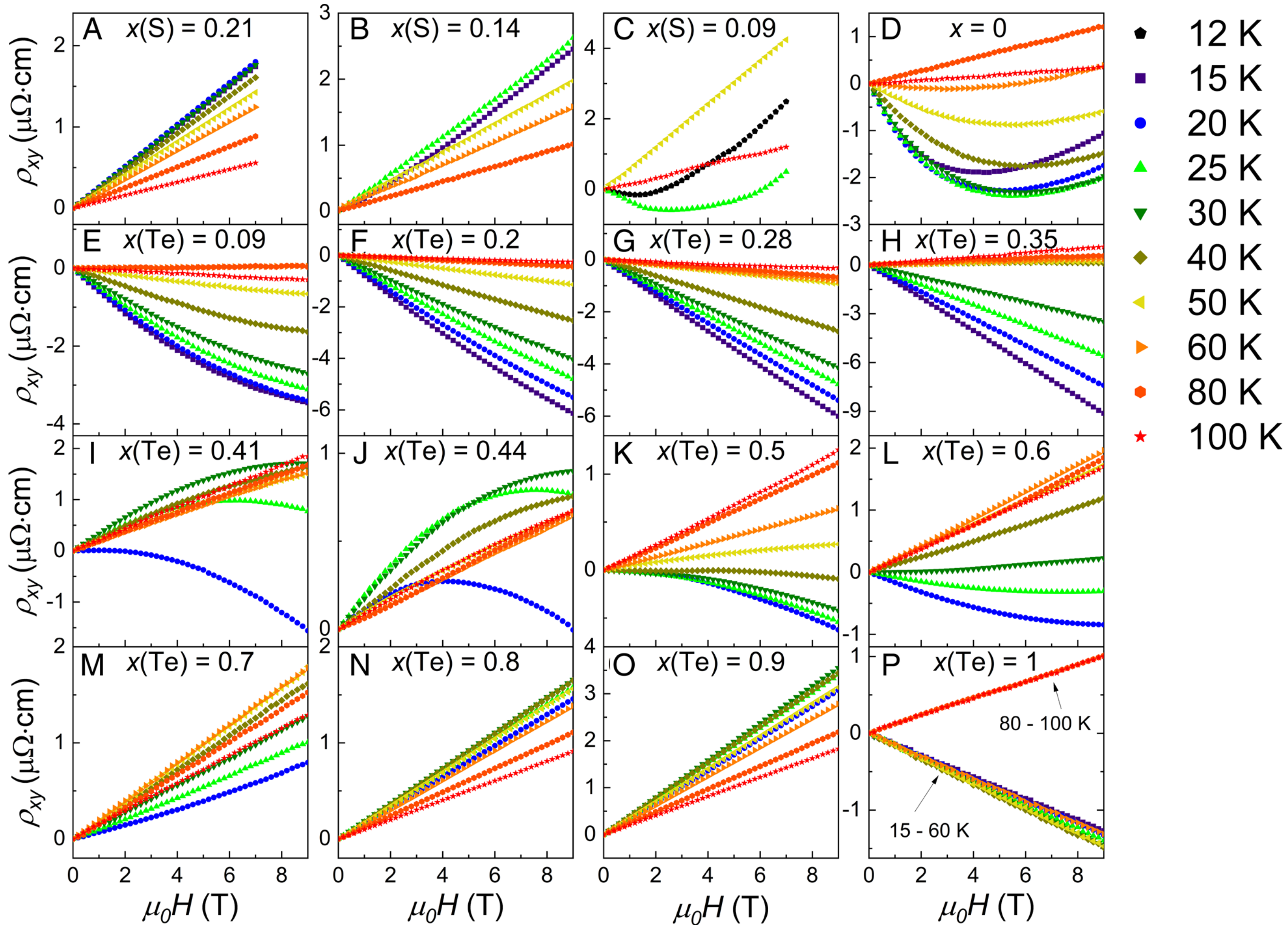

Fig. 2. Magnetic field dependence of Hall resistivity ρ_{xy} at different temperatures for $FeSe_{1-x}S_x$ ($0 < x \leq 0.21$) and $FeSe_{1-x}Te_x$ ($0 \leq x \leq 1$) single crystals. The data of $FeSe_{1-x}S_x$ ($0 < x \leq 0.21$) are from refs. 23, 48, and 49.

The first-order derivative of the MR to H clearly demonstrates the field-dependent behavior of MR. In the case of FeSe, the linear increase of d(MR)/dH with magnetic field at low fields indicates a classic B^2 dependence of the MR. The saturation of d(MR)/dH to a much reduced slope above a characteristic field B^* is typically attributed to the contribution of a linear field-dependent MR combined with a quadratic term. Linear MR is generally challenging to observe in normal materials because it requires large fields to reach the quantum limit, where all carriers occupy only the lowest Landau level (LL) (52, 53). However, in certain materials hosting Dirac fermions with linear energy dispersion, linear MR can be easily detected in low or moderate fields, which has been verified in many iron-based materials, such as $Ba(Sr)Fe_2As_2$ (50, 54), La(Pr)FeAsO (55, 56), FeSe (23), and $FeTe_{0.6}Se_{0.4}$ (40).

In the case of $FeSe_{1-x}S_x$ and $FeSe_{1-x}Te_x$, the saturation of d(MR)/dH is gradually suppressed with increasing x and completely disappears at x(S) = 0.21 and x(Te) = 0.28. However, when the doping level reaches x(Te) = 0.41, the saturation of d(MR)/dH reappears, and it maintains a constant value for $0.44 \leq x(\text{Te}) \leq 0.6$, indicating the dominance of the Dirac states. Importantly, it should be noted that the doping region where linear MR is observed coincides with the region where nonlinear ρ_{xy} is evident. The evolution of the Dirac states with S and Te doping from the Hall resistivity has been further confirmed by MR. Moreover, the violation of the Kohler's rule and the modified Kohler's rule provide further evidence for the multiband effects of the $FeSe_{1-x}Te_x$ system, as shown in *SI Appendix*, Figs. S5 and S6 (SI Appendix).

To investigate the multiband electronic structure of $FeSe_{1-x}S_x$ and $FeSe_{1-x}Te_x$ and distinguish between the bulk Dirac and the topological surface Dirac states, quantitative analysis is necessary. A three-band model was utilized for the regions of $0 \leq x(\text{Te}) \leq 0.2$ and $0.41 \leq x(\text{Te}) \leq 0.6$ (low-temperature regions with nonlinear Hall resistivity), considering two main carriers and one small carrier with high mobility. This model has been successfully applied to FeSe and $FeSe_{1-x}S_x$ and confirmed through ARPES measurements (26, 35, 48). Additionally, a two-band model was employed to analyze the linear Hall resistivity and corresponding MR for the regions with linear Hall resistivity. The fitting process and the typical results at 20 K [refer to *SI Appendix*, Fig. S7 and Table S1 (*SI Appendix*)] are shown in *SI Appendix*.

Fig. 4 illustrates the cloud diagram of carrier concentrations and mobility. The concentration of the main carriers, both hole and electron types, increases with temperature or S or Te doping, and remains nearly unchanged after the structural transition, as depicted in Fig. 4 *A* and *B* for hole and electron carrier concentrations, respectively. Therefore, the structural transition can be attributed as the primary factor influencing the change of carrier concentration. On the other hand, the mobility of the main carriers rapidly decreases in the low doping region, as shown in Fig. 4 *D* and *E*. For displaying the sign of the carriers, we define the mobility of hole carriers as positive and that of electron carriers as negative. Fig. 4*F* clearly shows the sign change behavior of the Dirac carriers with doping. The Dirac carrier concentration near x(Te) ~ 0.5 is significantly lower than that of FeSe (see Fig. 4*C*, where the Dirac carrier concentration near x(Te)

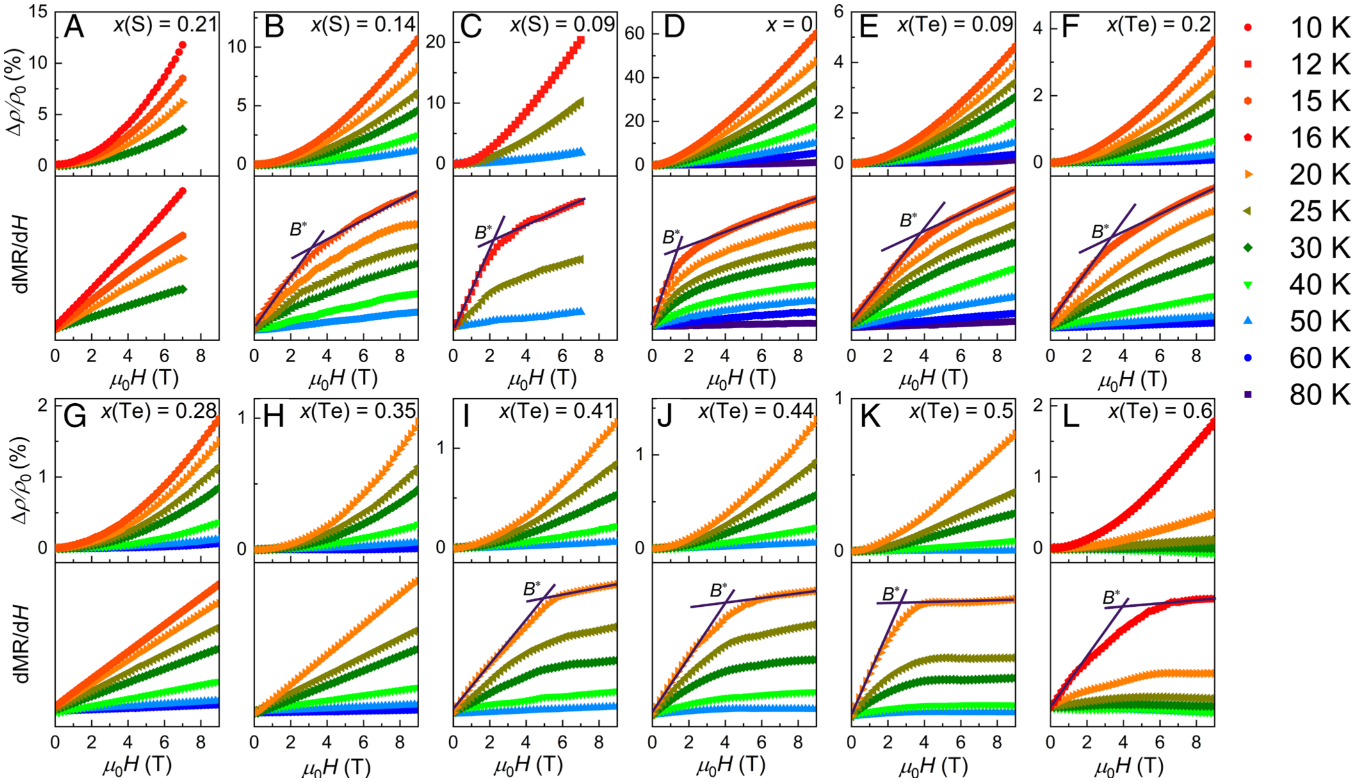

Fig. 3. Magnetic field dependence of MR [*Upper* panel of (*A*–*L*)] and the first-order derivative of MR to *H*, d(MR)/d*H* [*Lower* panel of (*A*–*L*)], at different temperatures for $FeSe_{1-x}S_x$ ($0 < x \le 0.21$) and $FeSe_{1-x}Te_x$ ($0 \le x \le 0.6$) single crystals. The data of $FeSe_{1-x}S_x$ ($0 < x \le 0.21$) are from refs. 23, 48, and 49.

~ 0.5 is magnified 10 times), but the mobility is comparable to that of FeSe (Fig. 4*F*). This observation is perfectly consistent with the fact of the bulk Dirac state around FeSe and the topological surface Dirac state around $FeSe_{0.5}Te_{0.5}$. The application of the three-band model has effectively quantitatively distinguished the bulk Dirac state from the topological surface Dirac state.

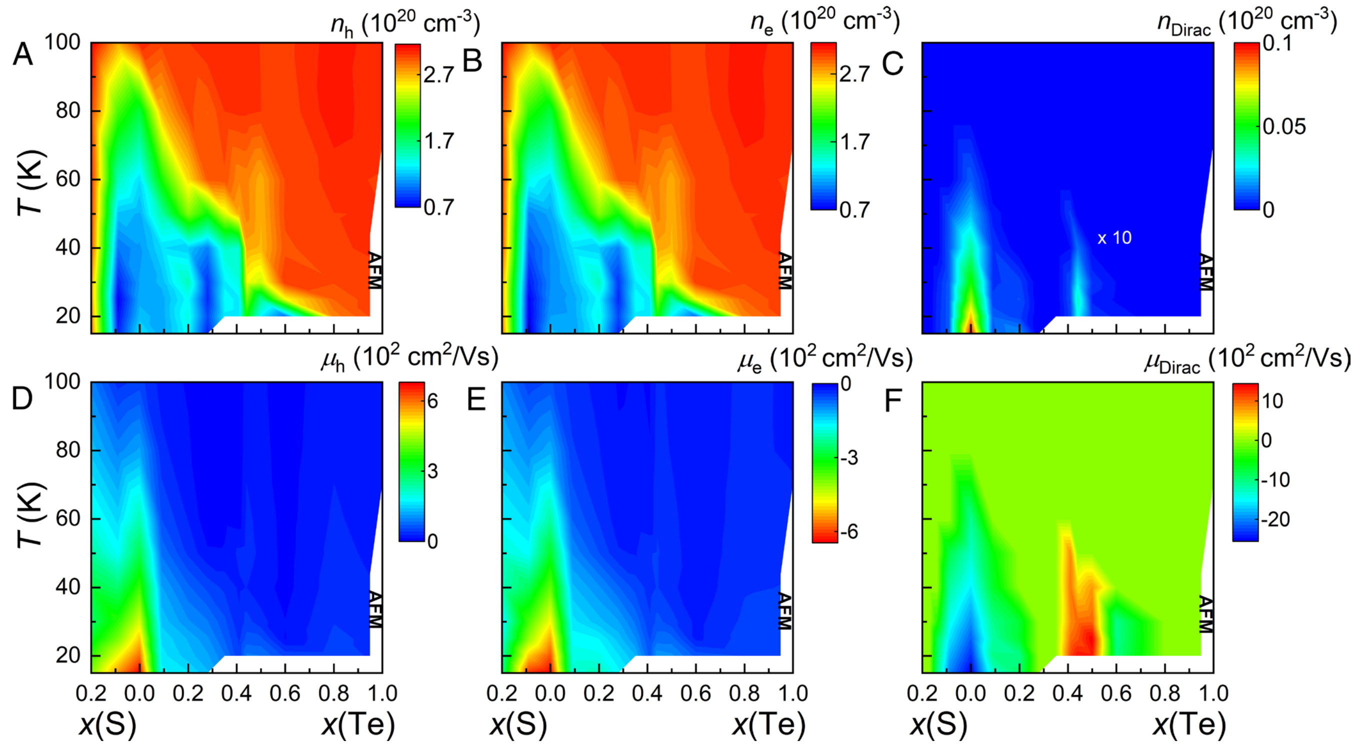

Fig. 4. The cloud diagrams of the main carrier concentrations with (*A*) hole, (*B*) electron type, and (*C*) Dirac carrier concentrations, and their corresponding mobilities in (*D*–*F*) for $FeSe_{1-x}S_x$ ($0 < x \le 0.2$) and $FeSe_{1-x}Te_x$ ($0 \le x \le 1$) single crystals. The Dirac carrier concentration near $FeSe_{0.5}Te_{0.5}$ in (*C*) is magnified 10 times. The mobility of hole carriers is defined as positive, and the mobility of electron carriers is defined as negative. The data of $FeSe_{1-x}S_x$ ($0 < x \le 0.2$) are from refs. 22, and 48.

Discussion

In order to illustrate the relationship between the transport properties, the Dirac states, and two superconducting domes, a phase diagram was constructed, incorporating T_c, the structural (nematic) transition temperature T_s, the Néel temperature T_N, T^*, and a contour plot of the power exponent n extracted from $d\ln(\rho - \rho_0)/d\ln T$ (Fig. 1). In $FeSe_{1-x}S_x$ ($0 < x \le 0.25$), the data points of T^* were extracted from our previous work (23) and ref. 22, and the other including T_c, T_s, and n are from refs. 16, 21, and 23–25. For FeSe, T_s and T^* occur nearly simultaneously at approximately 90 K, suggesting that the bulk Dirac state at the Brillouin zone corner seems to originate from the nematic phase. However, analysis of the mobility spectrum in FeSe contradicts this speculation, as a remarkable reduction in carrier number and an enhancement in carrier mobility were simultaneously observed below 120 K but above T_s, indicating the presence of another hidden order (34). $FeSe_{1-x}S_x$ exhibits a non-Fermi liquid behavior within the nematic phase. T_s and T^* also occur nearly simultaneously and disappear near the nematic QCP at x(S) = 0.17. Magetotransport properties of $FeSe_{1-x}S_x$ suggest that the Dirac states can be ascribed to the strange metal component (22). With Te doping, T^* gradually deviates from T_s toward lower temperatures, disappearing at x(Te) ~ 0.3, which corresponds to the junction of the two superconducting domes, forming a T_c-dip. Meanwhile, in the nematic phase, the normal state gradually transitions from non-Fermi liquid to Fermi liquid. The bulk Dirac states completely overlap with the strange metal states, accompanied by the superconducting dome SC1. More importantly, strange metal behavior above the superconducting dome SC1 is similar to the normal state resistivity in iron pnictides and cuprates superconductors, supporting the superconducting pairing mechanism connected to the AFM fluctuations.

The SC2 centers around the pure nematic QCP near x(Te) ~ 0.52. When x(Te) increases to ~0.41, the topological surface Dirac state appears due to the enhancement of SOC. It is worth noting that T^* is significantly higher than T_s, which is opposite to that of lower S or Te doping. Furthermore, although T_s vanishes at x(Te) ~ 0.5, T^* persists until x(Te) ~ 0.7. Fermi liquids also disappear with the reappearance of T^*, but the strange metals do not reappear, indicating that the topological surface Dirac state is different from the bulk Dirac state and has nothing to do with the strange metal. The rapid increase in T_c around x(Te) ~ 0.4 with the emergence of the topological surface Dirac state may originate from the topological superconductivity induced by the proximity effect of the topological surface Dirac state and the ordinary s-wave superconductor (57, 58). It is important that there is no non-Fermi liquid region above the SC2 similar to that above the SC1, which strongly supports the SC2 being associated with the QCP of the pure electronic nematic order. The metallicity of the normal state gradually deteriorates with Te doping, i.e., $n < 1$, which may be the normal state characteristic of the superconducting dome SC2 centered on the pure nematic QCP.

Another interesting phenomenon is that the topological surface Dirac states change sign near the pure nematic QCP. There are three schematic diagrams of the Dirac states in the *Top* panel of Fig. 1, showing the evolution of the Dirac states with S and Te doping. Near FeSe, the electron Dirac states at the Brillouin zone corner are bulk. With S or Te doping, the bulk Dirac state is gradually suppressed. Then, the topological surface Dirac state characterized by a band inversion along the Γ-Z line appears around x(Te) ~ 0.41 due to the enhancement of SOC. When crossing the nematic QCP around x(Te) ~ 0.52 (13, 14), the surface Dirac state changes from hole to electron, and that is, the Fermi surface crosses the Dirac point. The origin of the change is not yet clear, which may be related to the pure nematic QCP around x(Te) ~ 0.52. The topological surface Dirac states and topological superconductivity are the keys for further studying the pure nematic QCP and superconducting pairing mechanism.

Looking at the entire phase diagram, the normal state above SC1 far away from the long-range AFM order at FeTe exhibits a non-Fermi liquid state, but T_c is smaller than SC2 close to the AFM order, which is similar to the paradigm of the two superconducting domes in unconventional superconductors in ref. 12. However, the only difference is that in other unconventional superconductors, the superconducting dome with the non-Fermi liquid is generally higher than the other, and this anomaly in FeSe-based superconductors may be attributed to the topological superconductivity of SC2. The evolution of the Dirac states indicates that the appearance of the two superconducting domes may originate from the Fermi surface reconstruction with Te doping, similar to the quantum criticality transition in $K_{0.8}Fe_{2-x}Se_2$ (59) and the Lifshitz transition in the heavily K-deposed FeSe films (60). The two superconducting domes have completely different normal state resistivity and Dirac states, strongly supporting the possibility of two different superconducting pairing mechanisms.

In summary, we have successfully established the phase diagram with two superconducting domes in FeSe-based superconductors and provided the evolution of the Dirac states and normal state resistivity. Non-Fermi liquid appears on SC1, similar to iron pnictides and cuprates superconductors, supporting the superconducting pairing mechanism connected to the AFM fluctuations. The power exponents above SC2 are less than 1, suggesting a potential signature of superconducting pairing mediated by pure nematic fluctuations. The performance of the two superconducting domes in FeSe-based superconductors is similar to the paradigm of the two superconducting domes found in many other unconventional superconductors, implying the same natural properties.

There are three kinds of Dirac states, the topologically trivial bulk Dirac state at the Brillouin zone corner, accompanied by the SC1 near FeSe, the hole and electron topologically nontrivial surface Dirac states, accompanied by the SC2 near $FeSe_{0.5}Te_{0.5}$. The bulk Dirac states are closely related to the strange metal states and completely synchronized with them. The topological surface Dirac states undergo a sign change from hole to electron near the pure nematic QCP, providing important clues for understanding superconducting pairing mediated by pure nematic fluctuations. The junction of the two superconducting domes exhibits Fermi liquid behavior without the Dirac state. The evolution of these Dirac states indicates that the appearance of the two superconducting domes may originate from the Fermi surface reconstruction. The two superconducting domes exhibit completely different Dirac and normal transport behaviors, strongly supporting the possibility of two distinct superconducting pairing mechanisms.

Materials and Methods

$FeSe_{1-x}Te_x$ single crystals with $0 \le x \le 0.5$ were grown using the chemical vapor transport (CVT) method with a mixture of $KCl/AlCl_3$ as transport agents (19). $FeSe_{1-x}Te_x$ single crystals with $0.6 \le x \le 1$ were grown using self-flux method and excess Fe was removed through Te-vapor annealing (61, 62). X-ray diffraction (XRD) measurements were conducted using a Rigaku X-ray diffractometer with Cu-Kα radiation (λ = 1.54 Å). The elemental composition was determined using energy-dispersive X-ray spectroscopy (EDX). Electrical and magnetic transport measurements were performed using physical property measurement system (PPMS-9T, Quantum Design). For magnetotranport measurements, a six-probe method was employed to simultaneously measure Hall resistivity and MR. The magnetic field H was applied parallel to the c axis, perpendicular to the applied current. H was scanned from −9T to +9T and the data were processed as follows,

$\rho_{xy}(H) = (\rho_{xy}(+H) - \rho_{xy}(-H))/2$ and $\rho_{xx}(H) = (\rho_{xx}(+H) + \rho_{xx}(-H))/2$, which can effectively eliminate the longitudinal or transverse resistivity component caused by misalignment of the contacts.

Data, Materials, and Software Availability. All study data are included in the article and/or *SI Appendix*.

ACKNOWLEDGMENTS. This work was partly supported by the National Key R&D Program of China (Grant No. 2018YFA0704300), the National Natural Science Foundation of China (Grants Nos. 12374135, 12374136, 12204265, and 12204487), the Fundamental Research Funds for the Central Universities (Grants No. 2242024k30029), the open research fund of Key Laboratory of Quantum Materials and Devices (Southeast University), Ministry of Education, and the Natural Science Foundation of Shandong Province (Grant No. ZR2022QA040). The authors thank Peng Zhang for useful discussions and the Center for Fundamental and Interdisciplinary Sciences of Southeast University for the support in XRD and physical property measurements.

Author affiliations: [a]Key Laboratory of Quantum Materials and Devices of Ministry of Education, School of Physics, Southeast University, Nanjing 211189, China; [b]School of Physics and Physical engineering, Qufu Normal University, Qufu 273165, China; [c]School of Physics and Electronic Engineering, Jiangsu University, Zhenjiang 212013, China; and [d]Key Laboratory of Materials Physics, Institute of Solid State Physics, Hefei Institutes of Physical Science, Chinese Academy of Sciences, Hefei 230031, China

1. G. Grissonnanche *et al.*, Direct measurement of the upper critical field in cuprate superconductors. *Nat. Commun.* **5**, 3280 (2014).
2. R. A. Cooper *et al.*, Anomalous criticality in the electrical resistivity of $La_{2-x}Sr_xCuO_4$. *Science* **323**, 603 (2009).
3. Y. Koike *et al.*, Anomalous *x* dependence of T_c and possibility of low-temperature structural phase transition in $La_{2-x}Sr_xCu_{0.99}M_{0.01}O_4$ (M = Ni, Zn, Ga). *Solid State Commun.* **82**, 889 (1992).
4. L. Sun *et al.*, Re-emerging superconductivity at 48 kelvin in iron chalcogenides. *Nature* **483**, 67 (2012).
5. M. Hiraishi *et al.*, Bipartite magnetic parent phases in the iron oxypnictide superconductor. *Nat. Phys.* **10**, 300 (2014).
6. H. Q. Yuan *et al.*, Observation of two distinct superconducting phases in $CeCu_2Si_2$. *Science* **302**, 2104 (2003).
7. Y. Ando, S. Komiya, K. Segawa, S. Ono, Y. Kurita, Electronic phase diagram of high-T_c cuprate superconductors from a mapping of the in-plane resistivity curvature. *Phys. Rev. Lett.* **93**, 267001 (2004).
8. Y. Koike, T. Kawaguchi, N. Watanabe, T. Noji, Y. Saito, Superconductivity and low-temperature structural phase transition in $La_{1.98-x}Ce_{0.02}Ba_xCuO_4$. *Solid State Commun.* **79**, 155 (1991).
9. J. Yang *et al.*, New superconductivity dome in $LaFeAsO_{1-x}F_x$ accompanied by structural transition. *Chin. Phys. Lett.* **32**, 107401 (2015).
10. B. J. Ramshaw *et al.*, Quasiparticle mass enhancement approaching optimal doping in a high-Tc superconductor. *Science* **348**, 317 (2015).
11. H. Luetkens *et al.*, The electronic phase diagram of the $LaO_{1-x}F_xFeAs$ superconductor. *Nat. Mater.* **8**, 305 (2009).
12. T. Das, C. Panagopoulos, Two types of superconducting domes in unconventional superconductors. *New J. Phys.* **18**, 103033 (2016).
13. K. Ishida *et al.*, Pure nematic quantum critical point accompanied by a superconducting dome. *Proc. Natl. Acad. Sci. U.S.A.* **119**, e2110501119 (2022).
14. K. Mukasa *et al.*, Enhanced superconducting pairing strength near a pure nematic quantum critical point. *Phys. Rev. X* **13**, 011032 (2023).
15. Q. Wang *et al.*, Strong interplay between stripe spin fluctuations, nematicity and superconductivity in FeSe. *Nat. Mater.* **15**, 159 (2016).
16. P. Wiecki *et al.*, Persistent correlation between superconductivity and antiferromagnetic fluctuations near a nematic quantum critical point in $FeSe_{1-x}S_x$. *Phys. Rev. B* **98**, 020507 (2018).
17. J. P. Sun *et al.*, Dome-shaped magnetic order competing with high-temperature superconductivity at high pressures in FeSe. *Nat. Commun.* **7**, 12146 (2016).
18. K. Matsuura *et al.*, Maximizing T_c by tuning nematicity and magnetism in $FeSe_{1-x}S_x$ superconductors. *Nat. Commun.* **8**, 1143 (2017).
19. K. Mukasa *et al.*, High-pressure phase diagrams of $FeSe_{1-x}Te_x$: Correlation between suppressed nematicity and enhanced superconductivity. *Nat. Commun.* **12**, 381 (2021).
20. H.-H. Kuo, J.-H. Chu, J. C. Palmstrom, S. A. Kivelson, I. R. Fisher, Ubiquitous signatures of nematic quantum criticality in optimally doped Fe-based superconductors. *Science* **352**, 958 (2016).
21. X. Yi *et al.*, Hydrothermal synthesis and complete phase diagram of $FeSe_{1-x}S_x$ ($0 \le x \le 1$) single crystals. *Phys. Rev. B* **103**, 144501 (2021).
22. M. Čulo *et al.*, Putative Hall response of the strange metal component in $FeSe_{1-x}S_x$. *Phys. Rev. Res.* **3**, 023069 (2021).
23. Y. Sun, S. Pyon, T. Tamegai, Electron carriers with possible Dirac-cone-like dispersion in $FeSe_{1-x}S_x$ (x = 0 and 0.14) single crystals triggered by structural transition. *Phys. Rev. B* **93**, 104502 (2016).
24. M. Bristow *et al.*, Anomalous high-magnetic field electronic state of the nematic superconductors $FeSe_{1-x}S_x$. *Phys. Rev. Res.* **2**, 013309 (2020).
25. S. Hosoi *et al.*, Nematic quantum critical point without magnetism in $FeSe_{1-x}S_x$ superconductors. *Proc. Natl. Acad. Sci. U.S.A.* **113**, 8139 (2016).
26. M. D. Watson *et al.*, Emergence of the nematic electronic state in FeSe. *Phys. Rev. B* **91**, 155106 (2015).
27. S. Y. Tan *et al.*, Observation of Dirac cone band dispersions in FeSe thin films by photoemission spectroscopy. *Phys. Rev. B* **93**, 104513 (2016).
28. S. Licciardello *et al.*, Electrical resistivity across a nematic quantum critical point. *Nature* **567**, 7747 (2019).
29. P. Zhang *et al.*, Observation of topological superconductivity on the surface of an iron-based superconductor. *Science* **360**, 182 (2018).
30. P. Zhang *et al.*, Multiple topological states in iron-based superconductors. *Nat. Phys.* **15**, 41 (2019).
31. Z. Wang *et al.*, Topological nature of the $FeSe_{0.5}Te_{0.5}$ superconductor. *Phys. Rev. B* **92**, 115119 (2015).
32. M. Shimizu, N. Takemori, D. Guterding, H. O. Jeschke, Two-dome superconductivity in FeS induced by a Lifshitz transition. *Phys. Rev. Lett.* **121**, 137001 (2018).
33. J. P. Sun *et al.*, Reemergence of high-T_c superconductivity in the $(Li_{1-x}Fe_x)OHFe_{1-y}Se$ under high pressure. *Nat. Commun.* **9**, 380 (2018).
34. K. K. Huynh *et al.*, Electric transport of a single-crystal iron chalcogenide FeSe superconductor: Evidence of symmetry-breakdown nematicity and additional ultrafast Dirac cone-like carriers. *Phys. Rev. B* **90**, 144516 (2014).
35. M. D. Watson *et al.*, Dichotomy between the hole and electron behavior in multiband superconductor FeSe probed by ultrahigh magnetic fields. *Phys. Rev. Lett.* **115**, 027006 (2015).
36. J. P. Sun *et al.*, High-T_c superconductivity in FeSe at high pressure: Dominant hole carriers and enhanced spin fluctuations. *Phys. Rev. Lett.* **118**, 147004 (2017).
37. T. Shibauchi, T. Hanaguri, Y. Matsuda, Exotic superconducting states in FeSe-based materials. *J. Phys. Soc. Jpn.* **89**, 102002 (2020).
38. S. Kanayama *et al.*, Two-dimensional Dirac semimetal phase in undoped one-monolayer FeSe film. *Phys. Rev. B* **96**, 220509 (2017).
39. M. Yi *et al.*, Nematic energy scale and the missing electron pocket in FeSe. *Phys. Rev. X* **9**, 041049 (2019).
40. Y. Sun *et al.*, Multiband effects and possible Dirac fermions in $Fe_{1+y}Te_{0.6}Se_{0.4}$. *Phys. Rev. B* **89**, 144512 (2014).
41. T. M. McQueen *et al.*, Extreme sensitivity of superconductivity to stoichiometry in $Fe_{1+\delta}Se$. *Phys. Rev. B* **79**, 014522 (2009).
42. I. Pallecchi *et al.*, Seebeck effect in $Fe_{1+x}Te_{1-y}Se_y$ single crystals. *Phys. Rev. B* **80**, 214511 (2009).
43. Z. K. Liu *et al.*, Experimental observation of incoherent-coherent crossover and orbital-dependent band renormalization in iron chalcogenide superconductors. *Phys. Rev. B* **92**, 235138 (2015).
44. J. Huang *et al.*, Correlation-driven electronic reconstruction in $FeTe_{1-x}Se_x$. *Commun Phys* **5**, 29 (2022).
45. K. Okazaki *et al.*, Evidence for a $\cos(4\phi)$ modulation of the superconducting energy gap of optimally doped $FeTe_{0.6}Se_{0.4}$ single crystals using laser angle-resolved photoemission spectroscopy. *Phys. Rev. Lett.* **109**, 237011 (2012).
46. F. Chen *et al.*, Electronic structure of $Fe_{1.04}Te_{0.66}Se_{0.34}$. *Phys. Rev. B* **81**, 014526 (2010).
47. Y. Sun, T. Yamada, S. Pyon, T. Tamegai, Influence of interstitial Fe to the phase diagram of $Fe_{1+y}Te_{1-x}Se_x$ single crystals. *Sci. Rep.* **6**, 32290 (2016).
48. Y. A. Ovchenkov *et al.*, Highly mobile carriers in iron-based superconductors. *Supercond. Sci. Technol.* **30**, 035017 (2017).
49. W. K. Huang *et al.*, Non-Fermi liquid transport in the vicinity of the nematic quantum critical point of superconducting $FeSe_{1-x}S_x$. *Phys. Rev. Res.* **2**, 033367 (2020).
50. K. K. Huynh, Y. Tanabe, K. Tanigaki, Both electron and hole Dirac cone states in $Ba(FeAs)_2$ confirmed by magnetoresistance. *Phys. Rev. Lett.* **106**, 217004 (2011).
51. T. Liang *et al.*, Ultrahigh mobility and giant magnetoresistance in the Dirac semimetal Cd_3As_2. *Nat. Mater.* **14**, 280 (2015).
52. A. A. Abrikosov, Quantum linear magnetoresistance. *EPL* **49**, 789 (2000).
53. A. A. Abrikosov, Quantum magnetoresistance. *Phys. Rev. B* **58**, 2788 (1998).
54. S. V. Chong *et al.*, Large low-temperature magnetoresistance in $SrFe_2As_2$ single crystals. *EPL* **104**, 17002 (2013).
55. I. Pallecchi *et al.*, Magnetotransport in La(Fe, Ru)AsO as a probe of band structure and mobility. *Phys. Rev. B* **84**, 134524 (2011).
56. D. Bhoi, P. Mandal, P. Choudhury, S. Pandya, V. Ganesan, Quantum magnetoresistance of the PrFeAsO oxypnictide. *Appl. Phys. Lett.* **98**, 172105 (2011).
57. L. Fu, C. L. Kane, Superconducting proximity effect and Majorana fermions at the surface of a topological insulator. *Phys. Rev. Lett.* **100**, 096407 (2008).
58. D. Wang *et al.*, Evidence for Majorana bound states in an iron-based superconductor. *Science* **362**, 333 (2018).
59. J. Guo *et al.*, Pressure-driven quantum criticality in iron-selenide superconductors. *Phys. Rev. Lett.* **108**, 197001 (2012).
60. X. Shi *et al.*, Enhanced superconductivity accompanying a Lifshitz transition in electron-doped FeSe monolayer. *Nat. Commun.* **8**, 14988 (2017).
61. Y. Sun *et al.*, Evolution of superconductivity in $Fe_{1+y}Te_{1-x}Se_x$ annealed in Te vapor. *J. Phys. Soc. Jpn.* **82**, 093705 (2013).
62. Y. Sun, Z. Shi, T. Tamegai, Review of annealing effects and superconductivity in $Fe_{1+y}Te_{1-x}Se_x$ superconductors. *Supercond. Sci. Technol.* **32**, 103001 (2019).